

Charged particle transport in magnetic fields in EGSnrc

V. N. Malkov^{a)} and D. W. O. Rogers^{a)}

*Carleton Laboratory for Radiotherapy Physics, Physics Department, Carleton University,
Ottawa, Ontario K1S 5B6, Canada*

(Received 7 January 2016; revised 30 May 2016; accepted for publication 8 June 2016;
published 29 June 2016)

Purpose: To accurately and efficiently implement charged particle transport in a magnetic field in EGSnrc and validate the code for the use in phantom and ion chamber simulations.

Methods: The effect of the magnetic field on the particle motion and position is determined using one- and three-point numerical integrations of the Lorentz force on the charged particle and is added to the condensed history calculation performed by the EGSnrc PRESTA-II algorithm. The code is tested with a Fano test adapted for the presence of magnetic fields. The code is compatible with all EGSnrc based applications, including egs++. Ion chamber calculations are compared to experimental measurements and the effect of the code on the efficiency and timing is determined.

Results: Agreement with the Fano test's theoretical value is obtained at the 0.1% level for large step-sizes and in magnetic fields as strong as 5 T. The NE2571 dose calculations achieve agreement with the experiment within 0.5% up to 1 T beyond which deviations up to 1.2% are observed. Uniform air gaps of 0.5 and 1 mm and a misalignment of the incoming photon beam with the magnetic field are found to produce variations in the normalized dose on the order of 1%. These findings necessitate a clear definition of all experimental conditions to allow for accurate Monte Carlo simulations. It is found that ion chamber simulation times are increased by only 38%, and a $10 \times 10 \times 6 \text{ cm}^3$ water phantom with $(3 \text{ mm})^3$ voxels experiences a 48% increase in simulation time as compared to the default EGSnrc with no magnetic field.

Conclusions: The incorporation of the effect of the magnetic fields in EGSnrc provides the capability to calculate high accuracy ion chamber and phantom doses for the use in MRI-radiation systems. Further, the effect of apparently insignificant experimental details is found to be accentuated by the presence of the magnetic field. © 2016 American Association of Physicists in Medicine. [<http://dx.doi.org/10.1118/1.4954318>]

Key words: Monte Carlo, magnetic field, ion chamber, Fano test, EGSnrc

1. INTRODUCTION

The potential benefits of introducing external magnetic fields to radiation therapy have motivated a variety of studies. Shih¹ and Bielajew² explored the dose enhancing effects of magnetic fields in electron beams and found that the effects of the field can nearly double the maximum dose in water.³ Although photon beams do not directly experience the influence of the Lorentz force, electrons set in motion in the phantom will curve and can noticeably impact surface doses.⁴⁻⁷ This is known as the electron return effect and is noticeable in regions of abrupt density changes or localized magnetic fields. Additional perturbations in photon beams such as dose enhancement and reductions in penumbra dose have been established.^{2,8,9}

Several groups are developing synergistic MRI-radiation therapy machines for magnetic resonance guided radiation therapy (MRgRT) applications.^{8,10,11} These machines have variable beam energy, magnetic field magnitudes, and geometric configurations. In addition to the consequences of the magnetic field on dose distributions, the question of calibration and dosimetry in magnetic fields has arisen.¹²⁻¹⁴ Ion chamber and solid state detector responses per unit dose are found to vary by several percent in the presence

of a magnetic field when compared to the 0 T case.¹⁴⁻¹⁶ This necessitates the calculation of high precision correction factors, and reliable and accurate Monte Carlo techniques to handle the magnetic fields.

Currently, PENELOPE,¹⁷ MCNP5,¹⁸ and GEANT4 allow for charged particle transport in magnetic fields, but EGSnrc^{19,20} lost this capability in the transition from EGS4. A few groups have adapted the EGS4 magnetic field macros for use in EGSnrc.^{12,21} Essentially these changes apply the theory originally described by Bielajew.²² PENELOPE makes use of a similar algorithm and recent Fano tests demonstrate approximately 1% differences from the expected results.²³ This approach requires a significant reduction in step-size which can negatively impact the efficiency. GEANT4 has also been used to calculate ion chamber doses in the presence of magnetic fields,¹⁵ but there may be a significant drop in efficiency through the use of GEANT4.²⁴⁻²⁶

In this work, we implement charged particle transport in the presence of magnetic fields in EGSnrc. The new algorithm improves on the previous EGS4 magnetic field macros package, introduces a specialized single scatter (SS) algorithm, and allows for proper boundary crossing. The code is validated by a new Fano test that accommodates an external magnetic field.²⁷ Further, comparisons of calculated

to experimental ion chamber doses at magnetic fields ranging from 0 to 2 T are performed for various transport settings. Our ion chamber dose calculations agree in most cases with previous studies^{14,15} even for large step lengths in the EGSnrc calculations. Finally, we perform a timing study to demonstrate notable improvements in efficiency.

The main goal of this work is to produce a robust and reliable magnetic field transport algorithm which does not place overly strict restrictions on the step-size and allows for high accuracy ion chamber and other calculations. This will allow for detailed analysis of the effects of the magnetic field without compromising calculation time and permit the determination of detector calibration factors for use in MRI-radiotherapy systems.

2. METHODS

2.A. Lorentz force in a condensed history (CH) calculation

Charged particle transport in EGSnrc is performed by grouping a large number of interactions into several steps between discrete events (e.g., bremsstrahlung, knock-on electrons, etc.) which are accounted for an individual basis. EGSnrc uses an adaptive electron/positron stepping mechanism in which larger steps are calculated using a CH algorithm, PRESTA-II (default in EGSnrc), and a SS algorithm is used for short steps.^{28,29} In relation to the magnetic field code, the specialized case of the SS mode is given in the appropriate section below, and the PRESTA-II algorithm is outlined here. In a PRESTA-II step of length s , shown by the gray line in Fig. 1, the particle begins with an initial direction of motion, $\hat{u}(0)$, velocity, $\vec{v}(0)$, position, \vec{x}_o , and energy, E_o . Two scattering directions are sampled, $\hat{u}(s/2)$ and $\hat{u}(s)$, the directions at the middle and the end of the step, respectively. These direction vectors correspond to the velocities $\vec{v}(s/2)$ and $\vec{v}(s)$. The particle is transported to the position X_{CH} by the distance given by the original step length, s . The energy lost is computed on the basis of s , and the electron moves on to the next step (SS, CH, or a discrete event). This process is continued until the charged particle's energy falls below a user set energy (ECUT) at which point the particle's history is terminated and its remaining kinetic energy is deposited at its current position.

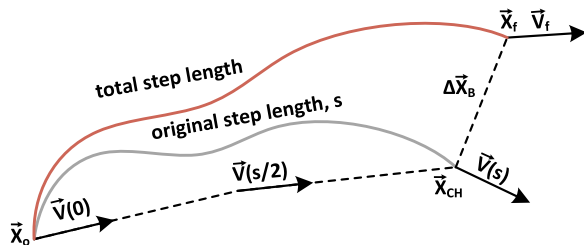


FIG. 1. Simplified EGSnrc PRESTA-II step in the presence of a magnetic field. The particle is initially at \vec{x}_o with velocity $\vec{v}(0)$, it is then transported a step length, s , to \vec{x}_{CH} by the CH algorithm which samples direction of motion at an intermediate, $\vec{v}(s/2)$, and final, $\vec{v}(s)$. $\Delta\vec{x}_B$ and $\Delta\vec{u}_B$ are calculated using Eqs. (2) and (6) to obtain the final position, \vec{x}_f , and velocity, \vec{v}_f .

To determine the influence of a magnetic field on a charged particle traveling in a material, the interplay between the medium's scattering and the Lorentz forces must be evaluated. Bielajew²² encoded this problem in the following general equation of motion:

$$\frac{d\vec{p}}{dt} = \vec{F}_{med}(E(t)) + \vec{F}_{em}(E(t), \vec{x}(t), \vec{u}(t)), \tag{1}$$

where \vec{p} is the momentum, t is the time, \vec{F}_{med} is the force on the particle due to the medium (i.e., elastic scattering), \vec{F}_{em} is the Lorentz force due to the external electric and magnetic fields, $E(t)$ is the energy, $\vec{x}(t)$ is the particle position, and $\vec{u}(t)$ is the particle's unit direction of motion. Bielajew placed this equation in the context of a CH step and demonstrated that in the case of no electric field the influence of the magnetic field on the direction of motion reduces to

$$\Delta\vec{u}_B(t) = \frac{qc^2}{v_o E_o} \int_0^t dt' \vec{v}(t') \times \vec{B}, \tag{2}$$

where $\Delta\vec{u}_B$ is the change in direction vector due to the magnetic field during a time period t , c is the speed of light, \vec{B} is the magnetic field, E_o is the particle's initial total energy, q is the particle's charge, $\vec{v}(t)$ is the particle velocity, and $v_o = |\vec{v}(0)|$. Under the assumptions of (i) little energy loss, (ii) a constant magnetic field, and (iii) minimal change in the direction of motion during the step, a one-point numerical integration (1-PI) technique can be used to evaluate Eq. (2) using

$$\Delta\vec{u}_{B1} = \frac{qtc^2}{v_o E_o} (\vec{v}(0) \times \vec{B}), \tag{3}$$

where the subscript $B1$ indicates that this is a one-point integration for the influence of the magnetic field. The above has been used by many groups as a convenient method for determining the effect of the magnetic field in a CH step and complies with the assumptions made originally by Bielajew.^{12,21} To account for energy loss and scattering during the step [i.e., weakening assumptions (i) and (iii)], the intermediate velocities in a PRESTA-II algorithm can be used to apply a three-point integration (3-PI) of Eq. (2) to give

$$\Delta\vec{u}_{B3} = \frac{qtc^2}{6v_o E_o} (\vec{v}(0) + 4\vec{v}(t/2) + \vec{v}(t)) \times \vec{B}, \tag{4}$$

where the subscript $B3$ indicates that this is a three-point integration (3-PI) for the influence of the magnetic field. Here the interaction of the magnetic field with the particle is sampled at three time positions which accommodates for the varying energy and direction of motion. $\vec{v}(t)$ is equal to $\vec{v}(s)$ in Fig. 1, and the velocity corresponding to $\vec{v}(s/2)$ is used as an approximation to the velocity at $t/2$. This assumption is used to facilitate the computation and, on average, is expected to be close enough to improve on the 1-PI technique.

To evaluate the time variable used in the numerical integration techniques, a two-point integration of the conventional time, velocity, and distance relationship using the initial, v_o , and final, v_f , velocities can be performed. This produces the

following expression for the time:

$$t \cong \frac{s}{v_o} \left(\frac{1}{2} + \frac{v_o}{2v_f} \right). \tag{5}$$

Using either integration method to obtain $\Delta\vec{u}_B$, the change in the position due to the magnetic field has been shown to be²²

$$\Delta\vec{x}_B = \frac{s\eta}{2} \Delta\vec{u}_B, \tag{6}$$

where the energy correction variable, η , is defined as the bracketed term in Eq. (5).

The influence of the magnetic field is added to the CH step as in Fig. 1. The position \vec{x}_{CH} is adjusted by adding $\Delta\vec{x}_B$ to obtain \vec{x}_f . The final velocity, \vec{v}_f , is determined by adding the change in the direction of motion due to the magnetic field, calculated using Eqs. (3) or (4), to the direction of $\vec{v}(t)$. To perform the addition and normalization of the direction vector properly, a procedure which adjusts the vector components perpendicular to the magnetic field while conserving the vector’s magnitude in the parallel direction is used (see Appendix A for details). Overall, PRESTA-II performs a regular CH step and the magnetic field influence is included after the CH calculations.

The three assumptions made above translate into step-size restriction parameters. Since a constant magnetic field is being considered and there are energy loss step-size control parameters in EGSnrc already, only the restriction on the change in the direction due to the magnetic field will be considered and encoded using:

$$\delta_u = |\Delta\hat{u}|, \tag{7}$$

recalling that $|\hat{u}| = 1$, makes δ_u a limit on the fractional change of the direction of motion produced by the magnetic field. Given a value for δ_u , Eqs. (3) and (7) are used to obtain the step-size limit,

$$s(B, \delta_u, E_o) = \frac{\delta_u \beta^2 E_o}{|q\vec{v}(0) \times \vec{B}|}, \tag{8}$$

where β is the particle velocity normalized by the speed of light and the η term is set to 1 so that this step-size quantity is consistent with other implementations which use a similar magnetic field transport theory. The 1-PI equation is used here since the scattering angles and energy loss over the step are required for the 3-PI method, and this necessitates knowledge of the step-size which Eq. (7) is used to determine. Appendix B provides a description of an additional limit on the step length which ensures that a CH step does not cause the particle to improperly transition into another region due to the addition of $\Delta\vec{x}_B$. These restrictions represent the maximum CH step that will be permitted in the magnetic field, and discrete events, boundaries, etc., will also restrict certain paths.

Using a δ_u of 0.02 has become common for Monte Carlo simulations which use similar theories, but this produces a potentially severe increase in computational time. The solution for a dose calculation in the presence of a magnetic field is expected to converge as δ_u decreases, and determining the largest possible δ_u that does not cause variations in the solution is required to improve efficiency. It is convenient to

make use of this parameter as a benchmarking tool of the stability and efficiency of the various transport options.

2.B. Scaled δ_u algorithm

The truncation error on a 3-PI is proportional to the fourth derivative of the function being integrated and to the fifth power of the step-size used to evaluate the integral.³⁰ Since a time independent magnetic field is simulated, the truncation error is directly proportional to the magnetic field. The error for a given step-size determined by Eq. (8) at a reference magnetic field, B_{ref} , will be halved for a calculation with $B = B_{ref}/2$. However, by Eq. (8), the permitted step-size with $B = B_{ref}/2$ in a CH calculation will be double that in the B_{ref} case, and the increase in the truncation error due to this larger step size will be a factor of 2^5 . To avoid fluctuation in truncation error at different magnetic fields, a scaling of the step-size with respect to the magnetic field is performed by using

$$s_{scale}(B) = s(B_{ref}, \delta_u, E_o) \left(\frac{B_{ref}}{B} \right)^{\frac{1}{5}}, \tag{9}$$

where $s_{scale}(B)$ is the scaled step-size, $s(B_{ref}, \delta_u, E_o)$ is evaluated using Eq. (8), and B is the magnetic field that the step-size is being sought at. Scaling with the fifth root is selected to account for the possibility of the error not being directly proportional to the magnetic field. Applying a fourth or sixth power scaling causes only about a 4% difference from the scaled step-size calculated by Eq. (9), which is relatively small compared to a doubling of the step-size if no scaling is used. The reference magnetic field and δ_u values are chosen based on Fano test calculations which produce accurate results. When this option is turned on, $s_{scale}(B)$ replaces the CH mode step-size restriction given in Eq. (8), and effectively attempts to maintain the error of the numerical method constant regardless of the strength of the B-field.

2.C. Adaptive integration algorithm

A downside of using 3-PI is a marked decrease in the efficiency of the overall simulation. An improvement in efficiency can be achieved by using an algorithm which utilizes 1-PI and 3-PI methods, depending on the step-size. The “Adaptive Integration” algorithm uses 1-PI whenever the step-size from other constraints is $\leq s_{min}$, evaluated with a δ_u of 0.05, since this is faster and accurate for small steps. Above s_{min} , the 3-PI is used to achieve better accuracy and s is capped at s_{max} , evaluated with a δ_u of 0.2. The values for the lower and upper δ_u values are chosen on the basis of Fano test results.

2.D. Magnetic field influence in SS mode

The SS mode in EGSnrc was originally introduced to deal with boundary transitions and to improve the accuracy of small steps. In a regular SS step, without a magnetic field, the particle travels linearly in its initial direction of motion and has an elastic scattering event at its final position to determine

the resulting direction. In a magnetic field, an analytical expression for charged particle transport in a magnetic field in vacuum²² is used instead of applying an approximation to the transport by using Eqs. (2) and (6), and the linear transport of the particle is bypassed. This method facilitates boundary crossing and ensures nearly exact transport for the SS step.

2.E. Boundary crossing

Without a magnetic field, boundary crossing in EGSnrc is performed using linear steps in the SS mode, the default boundary crossing algorithm in EGSnrc. When a step-size, s , larger than the shortest perpendicular distance to the nearest boundary, t_{perp} , is to be taken within a distance of skin-depth (set to three elastic mean free paths by default) to a boundary, a `howfar` call is made to determine the distance to the boundary in the initial direction of motion, d_{HF} . If d_{HF} is smaller than s , the step is shortened and the boundary is crossed using linear transport. In the presence of a magnetic field, the particle's trajectory will curve and the final transport may leave the particle in the current region or farther in the new region than intended. This can cause incorrect region transitions and can lead to erroneous scoring. To properly transition the particle in a magnetic field, a specialized boundary crossing algorithm (BCA) is introduced, as shown in Fig. 2. This algorithm applies only to the SS mode, and the PRESTA-I BCA option of EGSnrc does not support magnetic fields at this time. When a step-size to the next scatter, s_o , larger than t_{perp} and within a skin-depth to a boundary is to be taken, the particle is transported a distance t_{perp} using the analytical expression for charged particle transport in a magnetic field in vacuum instead of performing a check using `howfar`. At the end of this step, a new perpendicular distance to the nearest boundary, $t_{\text{perp}2}$, is evaluated and the particle is transported further by this distance, making the total step length to this point $s_2 = t_{\text{perp}} + t_{\text{perp}2}$. The process of recalculating t_{perp} continues until a boundary is reached or the allowed total step length is found to be larger than s_o , to which the step-size is capped. A boundary is reached when t_{perp} is found to be below a specified cutoff value (encoded by the `$BCA_lin_buffer` macro with a default value of 10 nm). Here a small linear step is then

taken to transition into the next region, but the final direction of motion is determined using the analytical expressions. In the case when a region transition is not required, $\Delta\vec{x}_B$ is applied to the position when $|\Delta\vec{x}_B| < t_{\text{perp}}$ at the end of the linear transport. Different cutoff values were tested using ion chamber dose calculations. No effect on dose calculations is found for values below 1×10^4 nm. The conservative value of 10 nm is chosen to ensure accuracy since there is little effect on the timing.

2.F. NE2571 ion chamber simulations

All ion chamber simulations were performed using the EGSnrc Monte Carlo system with the `egs_chamber`³¹ application. Variance reduction techniques are used to conserve CPU time and all default parameters are maintained for the simulations with the exception of using the NIST bremsstrahlung cross sections. The photon and electron total energy thresholds were set to 10 and 521 keV, respectively.

To be consistent with the measurement setup of Meijssing *et al.*¹⁵ who used 2 ion chamber configurations, calculations were performed in a delrin cylinder with a length of 6.9 cm and diameter of 4.3 cm. A parallel 6 MV photon beam¹⁵ (Elekta SLi25 spectrum³²) incoming from the negative z -direction and a uniform magnetic field in the y -direction is simulated throughout the phantom using the new EGSnrc magnetic field package. Calculations, not presented here, with a 6 MV Varian Linac spectrum revealed no sensitivity of the final results to the choice of spectrum for the same energy. In the first configuration, CI, the ion chamber has its central axis perpendicular to both the magnetic field and the photon beam, i.e., the chamber's central axis lies in the x -direction. In the second configuration, CII, the ion chamber remains perpendicular to the magnetic field but is now parallel to the photon beam, i.e., the long axis of the chamber is in the z -direction. These geometrical configurations are shown in Fig. 3. The NE2571 ion chamber model used for these simulations has been previously described by La Russa *et al.*³³ With omission here of the stem geometry description, the chamber consists of an active air volume with a length of 24.0 mm and a radius of 3.14 mm, a solid aluminium electrode

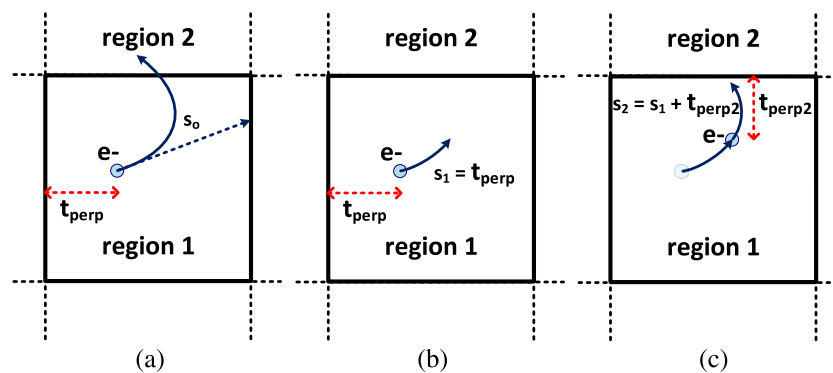


FIG. 2. Single scatter mode boundary crossing in the presence of magnetic fields. (a) An intended step larger than t_{perp} is to be taken. Linear (dashed) and magnetic field (solid) transport is shown. (b) The step-size is shortened to t_{perp} and the particle is transported using analytical solutions for magnetic field transport in vacuum. (c) A new t_{perp} is calculated, the step-size is increased by this amount and the particle is transported further.

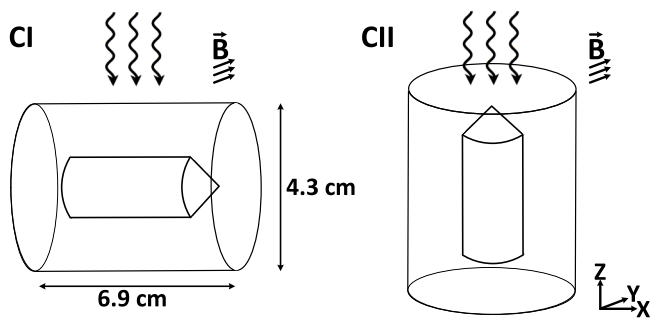


FIG. 3. Geometrical set up of ion chamber simulations with an incoming parallel 6 MV photon beam for configurations I and II (CI and CII). In both configurations the magnetic field is in the y -direction. A simplified ion chamber model is shown with the surrounding delrin build-up cap.

with a length of 20.5 mm and a radius of 0.5 mm, and a graphite wall with a thickness of 0.36 mm. The conical tip on the end of the chamber is also simulated.

The dose to the active volume of the chamber is scored as a function of magnetic field strength, ranging from 0 to 2 T in increments of 0.15 T. The dose is normalized by the dose obtained in the same geometry but in the absence of the magnetic field. Note that the normalization is performed using the original EGSnrc simulation package, which is defined as the NULL EGSnrc case. All dose values are calculated to below 0.02% statistical uncertainty. The values for both CI and CII configurations are compared to the experimental results obtained by Meijnsing *et al.*¹⁵ Testing is performed for the 1-PI and 3-PI with the new BCA and specialized SS mode turned on.

Configuration I was used to determine the impact of the magnetic field code on the simulation efficiency and timing. The normalized efficiency ($\varepsilon_{\text{norm}} = \varepsilon_o / \varepsilon_B$) and normalized time per history ($t_{\text{norm}} = t_B / t_o$) are reported for $\delta_u = 0.02$ and 0.2 for magnetic fields ranging from 0 to 3 T. Here ε_o and t_o represent the efficiency and time per history to complete the simulation for the NULL simulation (similarly ε_B and t_B are for the magnetic field case). The effect of δ_u on $\varepsilon_{\text{norm}}$ and t_{norm} is also studied for a 1.5 T magnetic field. All timing and efficiency simulation are performed with 1.5×10^7 histories on a single cpu core.

2.G. Fano cavity test

The Fano theorem has been used as a strict test of Monte Carlo algorithms. It states that as long as cross sections are independent of density and charged particle equilibrium exists, the electron spectrum is also independent of density.³⁴ To perform the test for a Monte Carlo code, a cavity region with a density 1000 times lower than the surrounding material²⁸ is used. In such tests, without a magnetic field, EGSnrc passes at the 0.1% level.²⁸ An alternative implementation of the Fano test was introduced by Sempau and Andreo³⁵ in which the photon beam is circumvented and a uniform intensity per unit mass source of electrons is simulated in two semi-infinite slabs of dense material with a gap of low density material in-between. By using the reciprocity theorem, a thin source of

electrons can be employed and the dose scored in the entire gas region. This test demonstrated that, with careful selection of transport parameters, the PENELOPE code passes the Fano test near the 0.1% level with deviations as high as 0.4% for certain configurations.³⁵

Bouchard and Bielajew³⁶ have demonstrated that the assumptions of the Fano cavity theorem are broken when a magnetic field is introduced. Bouchard *et al.*²⁷ introduced two alternative modifications to the Fano cavity test, either of which makes it valid in magnetic fields. The two alternatives are (1) using an isotropic uniform per unit mass source of electrons and (2) applying a magnetic field that scales with the mass density of the material. Pooter *et al.* implemented the first variant of the Fano cavity test in the PENELOPE code and observed variations near 1% for a 1.5 T magnetic field²³ for 4 MeV initial electron energy.

The first version of the magnetic field Fano test is implemented in the EGSnrc DOSRZnrc user code using the Sempau and Andreo Fano test approach. Two cylindrical geometries are simulated. In the first geometry (slab Fano test), a low density gas slab of thickness d_{gas} is placed between two slabs of the wall material each with thickness d_{wall} [see Fig. 4(a)]. The entire cylinder has a radius R equal to 1.4 times the CSDA range, R_{CSDA} , of the initial kinetic energy of the electrons in the gas. A thin, isotropic, uniform per unit mass electron source is simulated at the central axis. In the second geometry (ion chamber Fano test), Fig. 4(b), a gas cylinder of radius r_{gas} , set to 0.35 cm, and thickness d_{gas} is surrounded by the wall material having a total thickness T and radius R_{IC} , such that the distance between the gas region and the outer edges of the wall cylinder is at least d_{wall} . An isotropic uniform per unit mass electron source is simulated everywhere in the ion chamber Fano test geometry. In both geometries, d_{wall} is set to be 1.4 times the R_{CSDA} of the initial kinetic energy of the electrons in the wall. Gas thickness, d_{gas} , is simulated as 0.2 or 2 cm for the slab Fano test geometry, and 2 cm in the ion chamber Fano test. Graphite is used as the simulation material, with the wall having a density of 1.7 g cm^{-3} . The gas density is 1000 times less but with the same cross sections including the density effect as the wall. A magnetic field perpendicular to the central axis of the cylinders is simulated in both geometries. Electron kinetic energies of 0.01, 0.1, 1, and 10 MeV are simulated. Statistical uncertainties for the 10 MeV cases are

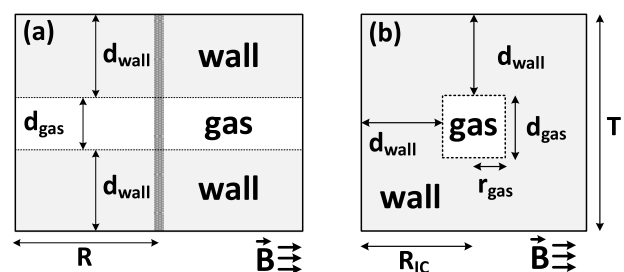


FIG. 4. (a) Cross section through the slab Fano test geometry. The shaded region in the center corresponds to the isotropic uniform per unit mass electron source. (b) Cross-section through the cylindrical ion chamber (IC) Fano test geometry. Electrons are generated isotropically on a per unit mass basis throughout the geometry.

below 0.09% and below 0.03% for all other energies. As required by this version of the Fano test, all photons produced in the simulation are terminated and their energy is deposited locally. The electron total energy threshold is set to 512 keV and secondary electrons are tracked as well. Dose, D , is scored in the gas regions of both geometries, and the ratio, Q , of the MC dose to the expected result, IE_o , is defined as

$$Q = \frac{D}{IE_o}, \tag{10}$$

where I is the number of electrons per unit mass and E_o is the initial kinetic energy of the source electrons. In the ideal case, Q would be equal to 1. For the slab Fano test geometry, the I variable in Eq. (10) is substituted with

$$I_{\text{slab}} = \frac{N}{R^2\pi(2d_{\text{wall}}\rho_{\text{wall}} + d_{\text{gas}}\rho_{\text{gas}})}, \tag{11}$$

where ρ_g and ρ_w are the gas and wall densities and N is the number of particle histories used for the calculation. For the ion chamber Fano test geometry, the I variable in Eq. (10) is:

$$I_{\text{IC}} = \frac{N}{\rho_{\text{wall}}\pi(TR_{\text{IC}}^2 - d_{\text{gas}}r_{\text{gas}}^2) + \rho_{\text{gas}}d_{\text{gas}}r_{\text{gas}}^2\pi}. \tag{12}$$

The slab Fano test is verified by calculating the degree of agreement EGSnrc has with the theoretical Fano value for the NULL field case. The ESTEPE variable, which sets the maximum fractional energy loss over a single CH or SS step, is varied from 0.01 to 0.25 to determine any step-size effects. To evaluate the effect of the magnetic field code, on both integration methods, a magnetic field ranging in magnitude from 0 to 5 T for δ_u values of 0.02 and 0.2 is simulated for the slab Fano test. Additionally, a study as a function of δ_u is performed for the 1.5 T case for both the slab and ion chamber Fano tests. The magnetic field is simulated perpendicular to the radial axis of the geometries as it was found that simulations with the parallel case pass the test more easily.

3. RESULTS AND DISCUSSION

3.A. Fano cavity test

Figure 5 shows the percent deviation of the MC calculated Fano dose from the theoretical value for the NULL field case as a function of ESTEPE for the 0.2 and 2 cm thick gas region. These simulations are run with the default XIMAX value and with isotropically radiating electrons from the source region. In all cases, deviations fall below the 0.1% threshold. The ESTEPE = 0.25 case corresponds to the default EGSnrc setting, i.e., no tuning of transport parameters is needed to pass. These results are in agreement with Fano tests performed with ion chambers in photon beams.^{20,37}

With the magnetic field on, Fig. 6 provides the percent deviation from the theoretical Fano test result for the 0.2 cm gas gap thickness for the 1-PI and 3-PI methods. At low δ_u values, for both integration techniques, the results are within the 0.1% range; however, large deviations are seen in the 1-PI calculations at higher δ_u values. The 3-PI provides

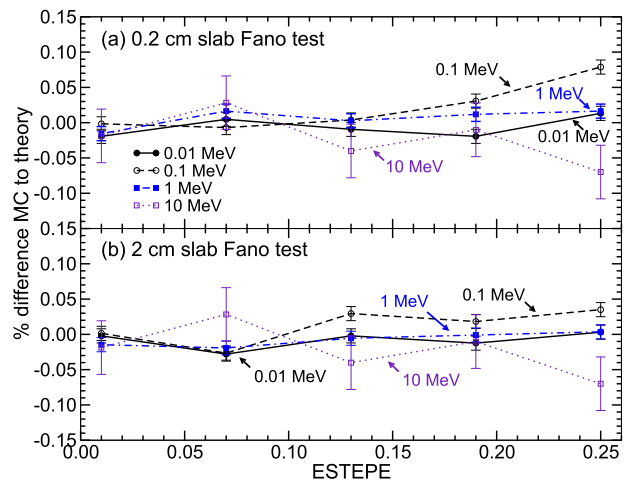


FIG. 5. Percent deviation of the Monte Carlo calculated Fano test dose from the theoretical value for the no magnetic field case as a function of the ESTEPE parameter for (a) 0.2 cm gas gap and (b) 2 cm gas gap.

improved stability even to δ_u values as high as 0.4. Figure 7 is the same study but for a 2 cm gas gap thickness. Again, agreement on the order of 0.1% is seen at a δ_u of 0.02, but the 1-PI results deviate from the expected results for the higher δ_u . Variations in the 3-PI results are observed for δ_u larger than 0.2; however, the differences are bounded by 0.25% for the 10 MeV case and 0.1% for the lower energies. The step-size dependence observed in the 2 cm case can be attributed to the increased number of particles having to be tracked to the outer radius of the Fano test geometry in the gas.

The results for the ion chamber (IC) Fano test are given in Fig. 8. The 3-PI results fall within 0.1% deviations from the theoretical value, while the 1-PI calculations do not exceed differences beyond 0.4%. These results are much better than the slab Fano test results and demonstrate that not all Fano test geometries are as rigorous a test of magnetic field Monte Carlo codes.

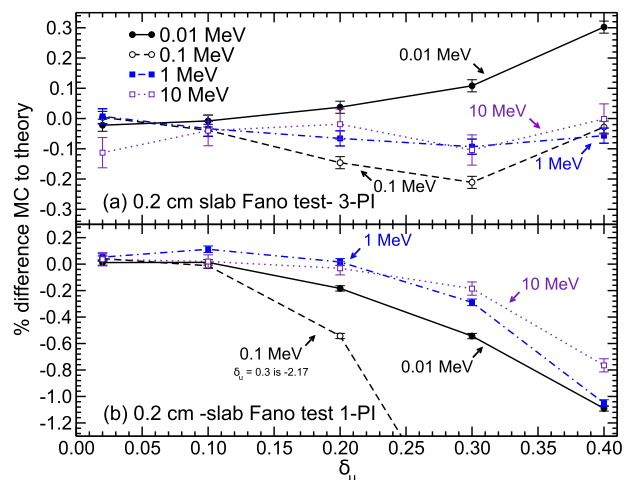


FIG. 6. Percent deviation of the Monte Carlo calculated Fano test dose from the theoretical value for the case of a uniform 1.5 T magnetic field parallel to the wall-gas interface with a 0.2 cm gas gap thickness. The (a) 3-PI and (b) 1-PI results are shown.

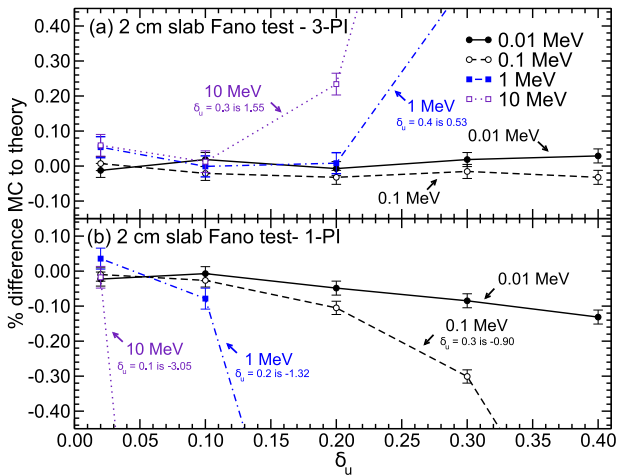


FIG. 7. Same as Fig. 6 but with a 2 cm gas gap.

Figure 9 demonstrates the dependence of the Fano test result on the magnitude of the magnetic field for the 0.2 and 2 cm gaps for a 1 MeV isotropic electron source. The 1-PI results in large deviations throughout the magnetic field range for a δ_u value of 0.2. An increase in the difference is seen for the 3-PI results at lower magnetic field values for a δ_u of 0.2. A δ_u of 0.1 eliminates the deviations. The variations at the higher δ_u are related to the improper scaling of the step-size restriction as a function of magnetic field. Applying the “Scaled δ_u ” algorithm with 1.5 T as the reference magnetic field and using a δ_u of 0.2 results in very good agreement with the Fano test. Turning on the scaled δ_u with or without the adaptive integration algorithms gives agreement within 0.1%, as seen in Fig. 9.

3.B. Ion chamber simulations

Figures 10 and 11 provide the NE2571 cavity doses in magnetic fields in the range of 0–2 T for configurations I and II normalized by the NULL EGSnrc cavity dose. Unless the specific algorithm is indicated, the calculations are performed

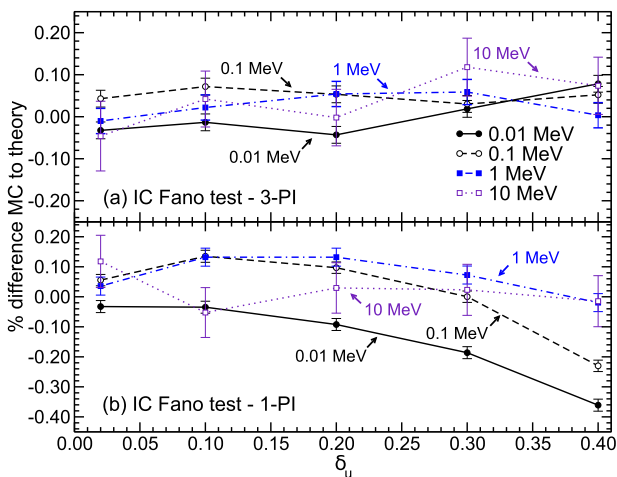


FIG. 8. Percent deviation of the Monte Carlo calculated IC Fano test dose from the theoretical value for a 0.35 cm radius and 2 cm thick gas region. The (a) 3-PI and (b) 1-PI results are shown.

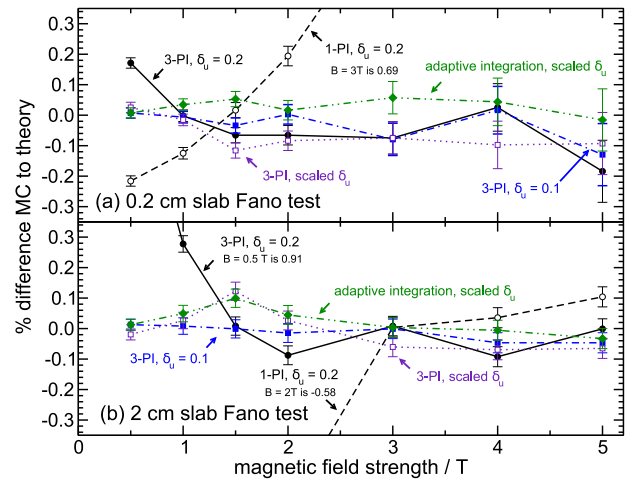


FIG. 9. Percent deviation of the Monte Carlo calculated Fano test dose from the theoretical value as a function of magnetic field for the (a) 0.2 cm and (b) 2 cm thick gas region with a 1 MeV isotropic electron source.

with the adaptive integration and scaled δ_u options turned on (“Full algorithm”). The experimental data, marked with diamonds, are from the work of Meijnsing *et al.*¹⁵ At a δ_u of 0.02 the two integration techniques agree with each other. The 3-PI does not change with a $\delta_u=0.2$, which does not hold true for the 1-PI. These findings are consistent with the Fano test results, where the 1-PI was determined to be unstable at higher δ_u values. From this, we determine that a δ_u of 0.2 is sufficiently stable for the 3-PI and use these setting for all subsequent ion chamber calculations.

Reasonable agreement with experiment is seen up to magnetic field values of 1.0 T, at which point a slight deviation is observed. Meijnsing *et al.*¹⁵ proposed that a tilt in the incoming beam with respect to the magnetic field lines may have caused a change in the ion chamber doses, but the authors could not verify if a tilt was present. We confirm that a 3° variation in the incoming beam results in deviations of the normalized dose curve from the 0° case, and find that a +3° degree tilt produces improved agreement with the experiment

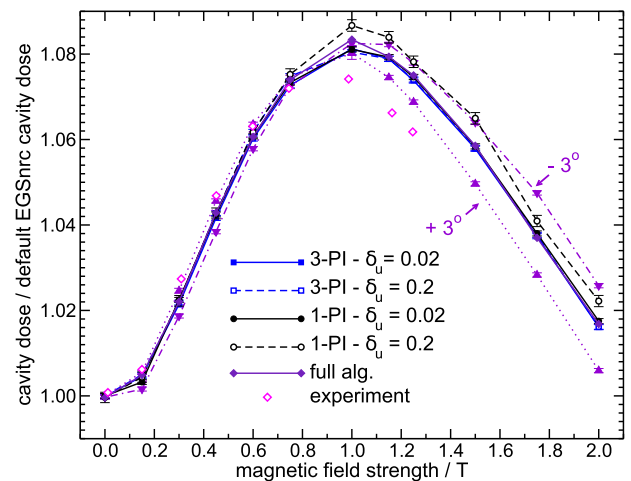


FIG. 10. Configuration I (see Fig. 3) NE2571 cavity dose as a function of magnetic field strength normalized by the NULL EGSnrc cavity dose. Experimental data are from Meijnsing *et al.* (Ref. 15).

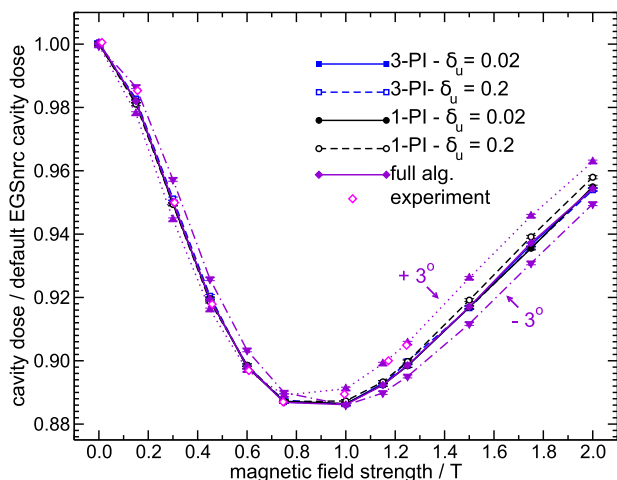


FIG. 11. Same as Fig. 10 but for configuration II.

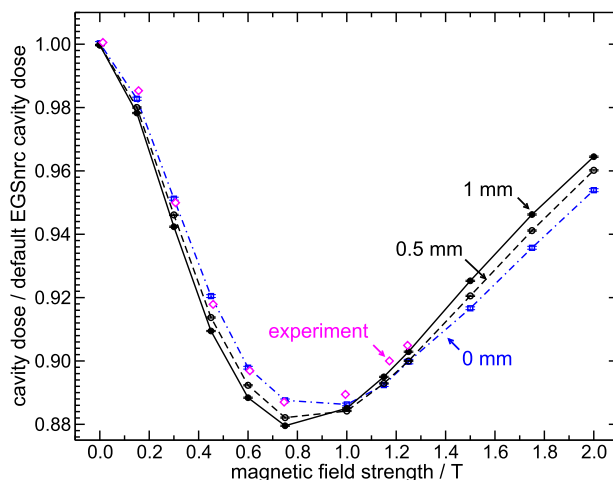


FIG. 13. Same as Fig. 12 but for configuration II.

for both CI and CII geometries. Further, small variations, within a few degrees, in the alignment of the ion chamber axis with respect to the photon beam do not produce changes in the dose response for a given magnetic field.

An additional unknown in the experimental setup is the possible presence of air gaps around the graphite walls of the chamber.³⁸ High density media dampen the effect of the deflection caused by the magnetic field, and a substitution with a low density medium like air can have a noticeable effect on the electron trajectories. The normalized ion chamber doses are calculated for a uniform 0.5 or 1.0 mm air gap around the walls of the ion chamber, including the conical tip, and are presented in Figs. 12 and 13 where each of the cavity dose curves as a function of magnetic field are normalized by the NULL EGSnrc simulation (no *B*-field) with the corresponding air gap around the chamber. In the NULL case, the introduction of a 1.0 mm air gap causes a 0.2% increase for CI and less than a 0.1% increase for CII. Variations on the order 1.0% or lower are seen for both air gap sizes in the magnetic field cases, with the 1.0 mm gap producing a more pronounced

effect. For CI, at magnetic fields below 1.0 T, the air gaps produce an increase in the chamber response. In the range of approximately 0.9–1.0 T, the effect of the air gap decreases and a reduction in the dose is observed for higher magnetic fields. This situation is reversed for CII, where an initial reduction in the dose is seen with a subsequent increase. These effects are a product of a balance of electrons being swept into or out of the chamber’s sensitive volume as a function of magnetic field.

The complexity introduced by the magnetic field accentuates experimental details that might otherwise appear to be inconsequential. Very detailed experimental descriptions are required to provide corresponding accurate Monte Carlo results.

3.C. Timing studies

The computational penalties for running the magnetic field code are explored. First, it is important to understand that an underlying variation in the computational time can occur due to changes in electron trajectories induced by the magnetic field. The effect of the trajectory on the time is not explicitly determined, but instead the effect of the various magnetic field transport options and algorithms as a function of step-size and magnetic field strength are evaluated.

Figure 14 provides the normalized efficiency and timing for the CI NE2571 ion chamber in delrin geometry with a 1.5 T magnetic field for 1-PI and 3-PI methods as a function of δ_u . Since the ratio of the uncertainties for the 1.5 T and NULL simulations remains constant for all δ_u , the normalized timing is always a constant ratio to the corresponding efficiency for the respective integration techniques. Due to the increased computational complexity of the 3-PI method, the time for this algorithm is notably higher than for the 1-PI method. A greater difference in the normalized timing with reducing δ_u is seen because of the increase in the number of steps taken. A low δ_u value such as 0.02 incurs a penalty in the range of 2–3 times the NULL EGSnrc case for both the timing and the efficiency for either integration approaches. Consequently, the use of a higher δ_u is desirable to reduce the timing cost. A δ_u above 0.1 achieves the majority of the reduction in timing increase.

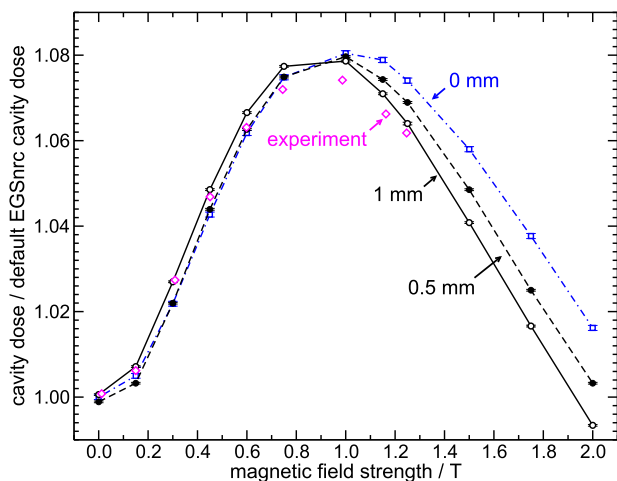


FIG. 12. Configuration I NE2571 cavity dose with air gaps around the wall of the chamber as a function of magnetic field strength normalized by the NULL EGSnrc.

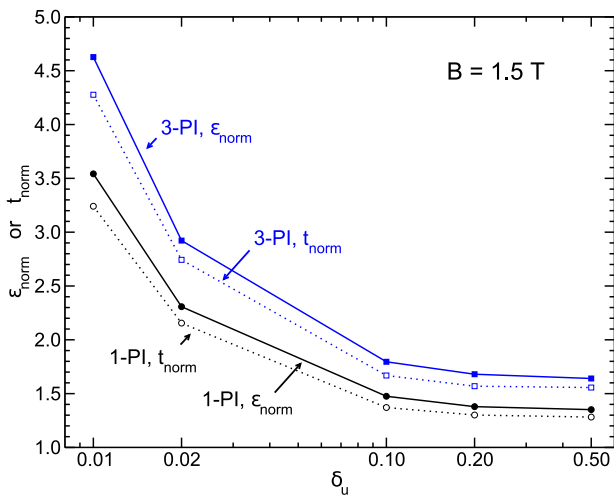


FIG. 14. Relative timing and efficiency for an NE2571 ion chamber in a delrin phantom in CI in the presence of a 1.5 T magnetic field as a function of δ_u . Values are normalized by the same calculation without the magnetic field, $t_{norm} = t_B/t_o$ and $\epsilon_{norm} = \epsilon_o/\epsilon_B$.

Drawing from the ion chamber dose calculation and the Fano test results, a δ_u of 0.2 is selected as the recommended value for the 3-PI calculations. Based on this δ_u , a purely 3-PI simulation at 1.5 T would take 56% longer to run with a corresponding 36% drop in efficiency as compared to the NULL field simulation.

The effect of the magnitude of the magnetic field on the normalized timing and efficiency for the ion chamber simulation is given in Fig. 15. The timing and the efficiency have a strong dependence on the magnetic field for a δ_u of 0.02. At a 3 T field, a threefold increase in the time is incurred even for the 1-PI. Moving to a δ_u of 0.2 reduces the dependence of the timing on the magnetic field. The statistical uncertainty in the simulation is independent of the choice of δ_u and is closely tied to the magnetic field used. The uncertainty increases gradually by approximately 12%

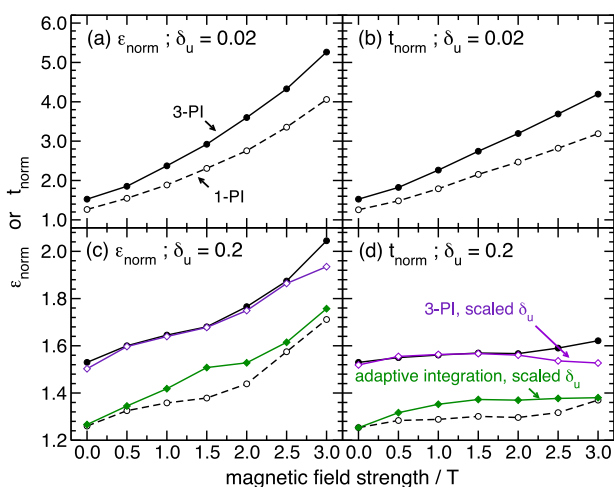


FIG. 15. Normalized (as in Fig. 14) timing and efficiency for an NE2571 ion chamber in a delrin phantom for δ_u of 0.02 and 0.2 as a function of magnetic field. Symbol meaning is maintained through (a)–(d). (a) and (c) are normalized efficiency and (b) and (d) are normalized timing.

between the 0 and 3 T case. The variation in the uncertainty is likely related to an increased variability in track length with increasing magnitude fields. To reduce the previously quoted increase in time with the 3-PI method at a δ_u of 0.2, the adaptive integration and scaled δ_u algorithms are also tested. The scaled δ_u algorithm reduces the dependence of the timing on the magnitude of the magnetic field. The adaptive integration algorithm makes use of the best of the two integration methods, since it applies the accuracy of the 3-PI when needed and suffers only a 38% increase in simulation time at higher magnetic fields while maintaining accuracy.

A timing comparison was also performed for a $10 \times 10 \times 6 \text{ cm}^3$ phantom with $(3 \text{ mm})^3$ voxels with DOSXYZnrc. A 1.5 T magnetic field is aligned perpendicular to the beam axis and directed along the negative z -direction. The entire phantom is filled with water. In this case, the increase in the computational time is 48% compared to the NULL EGSnrc simulation with ECUT set to 861 keV, range rejection applied to electrons below 2 MeV, and a photon splitting factor of 10. In the second test, the first 3 cm of the phantom is filled with water and the rest with air. There is a 76% increase in the simulation time compared to the NULL EGSnrc simulation for the same phantom with an ECUT of 611 keV. This difference in the increase in the computation time is attributed to the increased electron path length permitted in the air, which is affected more by the step-size restrictions implemented in the magnetic field code. Running on a single core of a 24 core Intel Xeon E5-2680 v3 2.50 GHz CPU machine, the CI simulations take approximately 6.3 s to achieve 2% uncertainty for the NULL case while a 1.5 T magnetic field simulation with the adaptive integration and scaled δ_u algorithms turned on with a reference field of 1.5 T takes 9.4 s to obtain the same uncertainty. A simulation with a $(30 \text{ cm})^3$ water phantom with $(3 \text{ mm})^3$ voxels and a $4 \times 4 \text{ cm}^2$ 6 MV photon beam coming in from the negative- z direction on the same machine takes 30 min for the NULL case and 44 min for a 1.5 T magnetic field in the y -direction (Adaptive Integration and Scaled δ_u turned on) to achieve 2% along the central axis.

4. CONCLUSION

Transport of charged particles in magnetic fields has been implemented in the EGSnrc code for the use of high accuracy ion chamber and phantom calculations. The extension code can be implemented by including an additional set of macros when compiling an application. This magnetic field extension code has been validated by the Fano test as applied in a magnetic field and has been found to agree with the expected results at the 0.1% level. The increase in the computational time due to running the code was found to be approximately 38% for ion chamber simulations and between 45% and 80% for a $(3 \text{ mm})^3$ phantom geometry. The increase in simulation time is found to be geometry dependent. It is well below the increase which would be incurred by the use of small step-sizes as in previous implementations.

NE2571 ion chamber simulations are performed and agreement with experimental data¹⁵ is found at magnetic fields

below 1 T. We have found that the air gaps around the chamber can induce variations in the normalized dose response on the order 1%. The tilt of the incoming beam with respect to the magnetic field can also influence the ion chamber reading. Detailed experimental descriptions are required to adequately simulate all of the physical effects induced by the magnetic field.

This efficient incorporation of the effect of the magnetic field into the EGSnrc code can now be used for determining correction factors for ion chamber measurement in hybrid MRI-radiotherapy systems.

ACKNOWLEDGMENTS

The authors thank Marc Chamberland for helpful comments on the paper and the referees for their helpful suggestions and comments. This work is supported by OGSST and QEII scholarships held by V. N. Malkov, NSERC, and Compute Ontario and the Compute/Calcul Canada computing platform via SHARCNET.

CONFLICT OF INTEREST DISCLOSURE

The authors have no COI to report.

APPENDIX A: NORMALIZATION OF FINAL DIRECTION VECTOR

Once $\Delta\vec{u}_B$ is determined, it must be added to the direction of motion at the end of the CH step and the unit vector properties of the direction of motion must be maintained. Previously proposed normalization techniques relied on adding the effect of the magnetic field and normalizing the resulting vector to unity, as in the following equation:

$$\hat{u}_f = \frac{\hat{u}_{CH} + \Delta\vec{u}_B}{|\hat{u}_{CH} + \Delta\vec{u}_B|}, \quad (\text{A1})$$

where, \hat{u}_f is the final direction of motion and \hat{u}_{CH} is the direction of motion at the end of the CH step. In this approach, components of the direction vector which should not be influenced by the magnetic field are scaled down in magnitude. The resulting effect is observed in Fig. 16(a), where motion in vacuum of a 0.5 MeV electron initially directed at a 45° angle with respect to the z -axis is tracked in a 0.2 T magnetic field oriented in the z -direction. Deviations from the analytical solution are observed for δ_u values as low as 0.02, and a noticeable change in the amplitude of oscillation due to the normalization problem is seen for $\delta_u = 0.1$. Calculations with $\delta_u = 0.2$ are not shown as the z -component of the direction became insignificant and particles traveled in perpetual circular orbits, i.e., trajectories did not reach past 10 cm depth along the z -axis.

To conserve the momentum in the direction parallel to the magnetic field, the components of the direction vector parallel and perpendicular to the magnetic field are defined as

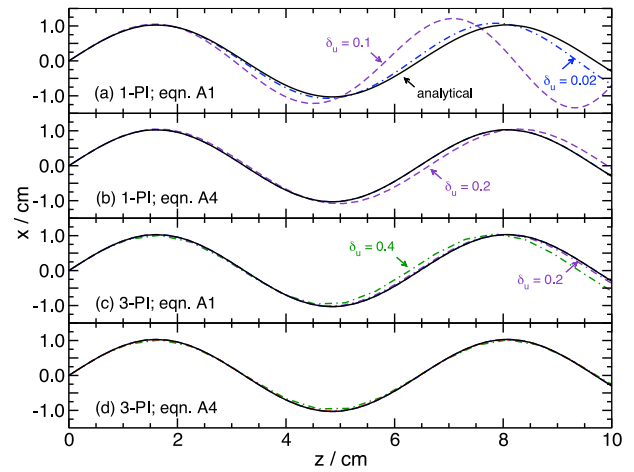


Fig. 16. x -axis as a function of z -axis position for a 0.5 MeV electron in a 0.2 T magnetic in z -direction in a near vacuum. The black line is the analytical solution. (a) 1-PI normalized with Eq. (A1), (b) as (a) but with Eq. (A4), (c) 3-PI normalized with Eq. (A1), (d) as (c) but with Eq. (A4).

$$\vec{u}_{\parallel} = \hat{u}_{CH} \cdot \hat{B}, \quad (\text{A2})$$

$$\vec{u}_{\perp} = \hat{u} - \vec{u}_{\parallel}, \quad (\text{A3})$$

where \hat{B} , \vec{u}_{\parallel} , and \vec{u}_{\perp} are the unit direction of the magnetic field, and the parallel and perpendicular components of the direction of motion, respectively. The effect of the magnetic field is obtained by using the individual magnitudes of these two components as in Eq. (A4),

$$\hat{u}_f = \vec{u}_{\parallel} + \frac{\vec{u}_{\perp} + \Delta\vec{u}_B}{|\vec{u}_{\perp} + \Delta\vec{u}_B|} |\vec{u}_{\perp}|. \quad (\text{A4})$$

This normalization is applied in Fig. 16(b) for the same energy and configuration as before. Here the $\delta_u = 0.02$ CH solution follows the analytical solution perfectly. Slight deviations are observed for $\delta_u = 0.2$. Using 3-PI, the $\delta_u = 0.2$ solution also maintains adherence to the analytical propagation [Fig. 16(d)]. Further, using 3-PI appears to overcome the issues presented by using Eq. (A1) [Fig. 16(c)], but the appropriate normalization technique is applied for increased stability in the solution.

The component normalization technique provides improved tracking of particles in vacuum, and in low density media. Coupled to the higher order integration technique a larger value for the δ_u parameter is permissible, which corresponds to larger step-sizes and shorter computational times.

APPENDIX B: CONDENSED HISTORY t_{perp} RESTRICTION

Since boundary crossing is mediated by SS, the CH mode cannot cause regional transitions. Without the magnetic field code, the CH step is restricted to a maximum value of t_{perp} . If a magnetic field is present and Eq. (6) is used to adjust the position at the end of the CH step, the particle can step into an incorrect region even if the CH total step length was just t_{perp} [see Fig. 17(a)]. To maintain proper boundary transitions, it is important that when a magnetic field is present

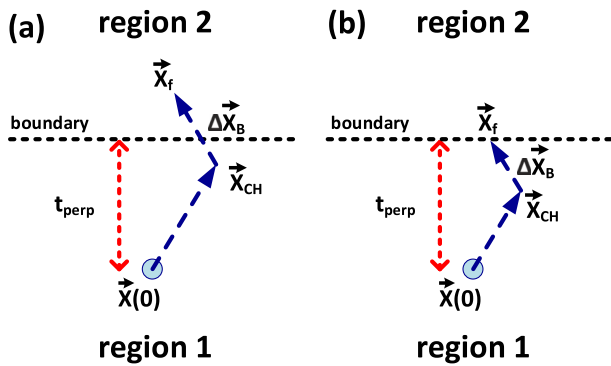


FIG. 17. A condensed history step equal to t_{perp} in a magnetic field (a). The influence of the magnetic field causes the particle to fall into region two. Restricting the step-size using Eq. (B3) ensure the final position is in region one (b).

the displacement caused by the magnetic field, $\Delta\vec{x}_B$, is added to the step length taken in the CH calculation, t_{CH} , and this must be bounded to t_{perp} , as in Fig. 17(b).

This is encoded as

$$t_{\text{perp}} = t_{\text{CH}} + |\Delta\vec{x}_B|. \quad (\text{B1})$$

Using Eq. (6) and $s = t_{\text{CH}}$, Eq. (B1) can be rewritten as

$$t_{\text{perp}} = t_{\text{CH}} + \frac{t_{\text{CH}}\eta}{2} |\Delta\vec{u}_B|. \quad (\text{B2})$$

Here, the value of η is estimated by using the ESTEPE variable, which controls the maximal fractional energy loss along a step in EGSnrc. Equation (3) is used to evaluate Δu_B and substitution into Eq. (B2) gives

$$t_{\text{perp}} = t_{\text{CH}} + t_{\text{CH}}^2 \left| \frac{q(\eta c)^2}{4E v_i} \vec{v}(0) \times \vec{B} \right|. \quad (\text{B3})$$

This is a quadratic equation which can be solved for t_{CH} values that satisfy the expression. The maximum value is used as the upper bound for the CH mode restriction. By using this algorithm, proper boundary transitions are maintained and no errors in scoring are encountered. Since the solution to the quadratic equation does not include any variation in velocity or direction of motion during the step, it is possible that the 3-PI results in a total step larger than t_{CH} . To avoid this, the magnitude of the change in position induced by the magnetic field is calculated and compared to the current t_{perp} value, and the 1-PI calculation is used if t_{perp} is found to be smaller. This type of event occurs fairly rarely and does not influence the overall dose calculation results.

^{a)}Electronic addresses: drogers@physics.carleton.ca and victormalkov@cmail.carleton.ca

¹C. C. Shih, "High energy electron radiotherapy in a magnetic field," *Med. Phys.* **2**, 9–13 (1975).

²A. F. Bielajew, "The effect of strong longitudinal magnetic fields on dose deposition from electron and photon beams," *Med. Phys.* **20**, 1171–1179 (1993).

³M. A. Earl and L. Ma, "Depth dose enhancement of electron beams subject to external uniform longitudinal magnetic fields: A Monte Carlo study," *Med. Phys.* **29**, 484–491 (2002).

⁴X. A. Li, L. Reiffel, J. Chu, and S. Naqvi, "Conformal photon-beam therapy with transverse magnetic fields: A Monte Carlo study," *Med. Phys.* **28**, 127–133 (2001).

⁵D. Jette, "Magnetic fields with photon beams: Monte Carlo calculations for a model magnetic field," *Med. Phys.* **27**, 2726–2738 (2000).

⁶C. Kirkby, T. Stanescu, S. Rathee, M. Carlone, B. Murray, and B. G. Fallone, "Patient dosimetry for hybrid MRI-radiotherapy systems," *Med. Phys.* **35**, 1019–1027 (2008).

⁷B. M. Oborn, P. E. Metcalfe, M. J. Butson, and A. B. Rosenfeld, "Monte Carlo characterization of skin doses in 6 MV transverse field MRI-Linac systems: Effect of field size, surface orientation, magnetic field strength, and exit bolus," *Med. Phys.* **37**, 5208–5217 (2010).

⁸B. W. Raaijmakers, A. J. E. Raaijmakers, A. N. T. J. Kotte, D. Jette, and J. J. W. Lagendijk, "Integrating a MRI scanner with a 6 MV radiotherapy accelerator: Dose deposition in a transverse magnetic field," *Phys. Med. Biol.* **49**, 4109–4118 (2004).

⁹A. J. E. Raaijmakers, B. W. Raaijmakers, and J. J. W. Lagendijk, "Magnetic-field-induced dose effects in MR-guided radiotherapy systems: Dependence on the magnetic field strength," *Phys. Med. Biol.* **53**, 909–923 (2008).

¹⁰B. G. Fallone, B. Murray, S. Rathee, T. Stanescu, S. Steciw, S. Vidakovic, E. Blosser, and D. Tymofichuk, "First MR images obtained during megavoltage photon irradiation from a prototype integrated Linac-MR system," *Med. Phys.* **36**, 2084–2088 (2009).

¹¹T. Kron, D. Eyles, J. L. Schreiner, and J. Battista, "Magnetic resonance imaging for adaptive cobalt tomotherapy: A proposal," *J. Med. Phys.* **31**, 242–254 (2006).

¹²C. Kirkby, B. Murray, S. Rathee, and B. G. Fallone, "Lung dosimetry in a Linac-MRI radiotherapy unit with a longitudinal magnetic field," *Med. Phys.* **37**, 4722–4732 (2010).

¹³M. Reynolds, B. G. Fallone, and S. Rathee, "Technical Note: Response measurement for select radiation detectors in magnetic fields," *Med. Phys.* **42**, 2837–2840 (2015).

¹⁴M. Reynolds, B. G. Fallone, and S. Rathee, "Dose response of selected ion chambers in applied homogeneous transverse and longitudinal magnetic fields," *Med. Phys.* **40**, 042102 (7pp.) (2013).

¹⁵I. Meijssing, B. W. Raaijmakers, A. J. E. Raaijmakers, J. G. M. Kok, L. Hogeweg, B. Liu, and J. J. W. Lagendijk, "Dosimetry for the MRI accelerator: The impact of a magnetic field on the response of a Farmer NE2571 ionization chamber," *Phys. Med. Biol.* **54**, 2993–3002 (2009).

¹⁶M. Reynolds, B. G. Fallone, and S. Rathee, "Dose response of selected solid state detectors in applied homogeneous transverse and longitudinal magnetic fields," *Med. Phys.* **41**, 092103 (12pp.) (2014).

¹⁷F. Salvat, J. M. Fernandez-Varea, J. Baro, and J. Sempau, "PENELOPÉ, a code system for Monte Carlo simulation of electron and photon transport," University of Barcelona Report, 2003.

¹⁸J. S. Bull, H. G. Hughes, P. L. Walstrom, J. D. Zumbro, and N. V. Mokhov, "Magnetic field tracking with mcnp5," *Radiat. Prot. Dosim.* **116**, 307–311 (2005).

¹⁹I. Kawrakow and D. W. O. Rogers, "The EGSnrc code system: Monte Carlo simulation of electron and photon transport," Technical Report PIRS–701, National Research Council Canada, Ottawa, Canada, 2006.

²⁰I. Kawrakow, "Accurate condensed history Monte Carlo simulation of electron transport. II. Application to ion chamber response simulations," *Med. Phys.* **27**, 499–513 (2000).

²¹Y. M. Yang and B. Bednarz, "Consistency evaluation between EGSnrc and GEANT4 charged particle transport in an equilibrium magnetic field," *Phys. Med. Biol.* **58**, N47–N58 (2013).

²²A. F. Bielajew, "Electron transport in \vec{E} and \vec{B} fields," in *Monte Carlo Transport of Electrons and Photons*, edited by T. M. Jenkins, W. R. Nelson, A. Rindi, A. E. Nahum, and D. W. O. Rogers (Plenum, New York, 1988), pp. 421–434.

²³J. A. de Pooter, L. A. de Prez, and H. Bouchard, "Application of an adapted Fano cavity test for Monte Carlo simulations in the presence of B-fields," *Phys. Med. Biol.* **60**, 9313–9327 (2015).

²⁴E. Poon, J. S. Seuntjens, and F. Verhaegen, "Consistency test of the electron transport algorithm in the GEANT4 Monte Carlo code," *Phys. Med. Biol.* **50**, 681–694 (2005).

²⁵S. Elles, V. N. Ivanchenko, M. Maire, and L. Urban, "GEANT4 and Fano cavity test: Where are we?," *J. Phys.: Conf. Ser.* **102**, 012009 (2008).

²⁶J. P. Archambault and E. Mainegra-Hing, "Comparison between EGSnrc, GEANT4, mcnp5 and Penelope for mono-energetic electron beams," *Phys. Med. Biol.* **60**, 4951–4962 (2015).

- ²⁷H. Bouchard, J. de Pooter, A. Bielajew, and S. Duane, "Reference dosimetry in the presence of magnetic fields: Conditions to validate Monte Carlo simulations," *Phys. Med. Biol.* **60**, 6639–6654 (2015).
- ²⁸I. Kawrakow, "Accurate condensed history Monte Carlo simulation of electron transport. I. EGSnrc, the new EGS4 version," *Med. Phys.* **27**, 485–498 (2000).
- ²⁹I. Kawrakow, E. Mainegra-Hing, D. W. O. Rogers, F. Tessier, and B. R. B. Walters, "The EGSnrc code system: Monte Carlo simulation of electron and photon transport," NRC Technical Report PIRS-701 v4-2-3-2 (National Research Council Canada, Ottawa, Canada, 2011), http://www.nrc-cnrc.gc.ca/eng/solutions/advisory/egsnrc/download_egsnrc.html.
- ³⁰R. Burden and J. Faires, *Numerical Analysis*, 9th ed. (Brooks/Cole, Boston, MA, 2011).
- ³¹J. Wulff, K. Zink, and I. Kawrakow, "Efficiency improvements for ion chamber calculations in high energy photon beams," *Med. Phys.* **35**, 1328–1336 (2008).
- ³²D. Sheikh-Bagheri and D. W. O. Rogers, "Monte Carlo calculation of 9 MV photon beam spectra using the BEAM code," *Med. Phys.* **29**, 391–402 (2002).
- ³³D. J. La Russa, M. McEwen, and D. W. O. Rogers, "An experimental and computational investigation of the standard temperature-pressure correction factor for ion chambers in kilovoltage x rays," *Med. Phys.* **34**, 4690–4699 (2007).
- ³⁴U. Fano, "Note on the Bragg-Gray cavity principle for measuring energy dissipation," *Radiat. Res.* **1**, 237–240 (1954).
- ³⁵J. Sempau and P. Andreo, "Configuration of the electron transport algorithm of PENELOPE to simulate ion chambers," *Phys. Med. Biol.* **51**, 3533–3548 (2006).
- ³⁶H. Bouchard and A. Bielajew, "Lorentz force correction to the Boltzmann radiation transport equation and its implications for Monte Carlo algorithms," *Phys. Med. Biol.* **60**, 4963–4971 (2015).
- ³⁷D. J. La Russa and D. W. O. Rogers, "Accuracy of Spencer-Attix cavity theory and calculations of fluence correction factors for the air kerma formalism," *Med. Phys.* **36**, 4173–4183 (2009).
- ³⁸D. J. O'Brien, S. L. Hackett, B. van Asselen, G. Ibbott, B. W. Raaymakers, G. O. Sawakuchi, and J. W. H. Wolthaus, "TH-CD-304-08: Small air-gaps affect the response of ionization chambers in the presence of a 1.5 T magnetic field," *Med. Phys.* **42**, 3724 (2015).